

---

# Hard-tail emission in the soft state of low-mass X-ray binaries and their relation to the neutron star magnetic field

Kazumi ASAI\*, Tatehiro MIHARA, Masaru MASTUOKA and Mutsumi SUGIZAKI

MAXI team, RIKEN, 2-1 Hirosawa, Wako, Saitama 351-0198, Japan

\*E-mail: kazumi@crab.riken.jp

Received ; Accepted

## Abstract

Average hard-tail X-ray emission in the soft state of nine bright Atoll low-mass X-ray binaries containing a neutron star (NS-LMXBs) are investigated by using the light curves of MAXI/GSC and Swift/BAT. Two sources (4U 1820–30 and 4U 1735–44) exhibit large hardness ratio (15–50 keV/2–10 keV:  $HR > 0.1$ ), while the other sources distribute at  $HR \lesssim 0.1$ . In either case,  $HR$  does not depend on the 2–10 keV luminosity. Therefore the difference of  $HR$  is due to the 15–50 keV luminosity, which is Comptonized emission. The Compton cloud is assumed to be around the neutron star. The size of the Compton cloud would affect the value of  $HR$ . Although the magnetic field of NS-LMXB is weak, we could expect a larger Alfvén radius than the innermost stable circular orbit or the neutron star radius in some sources. In such cases, the accretion inflow is stopped at the Alfvén radius and would create relatively large Compton cloud. It would result in the observed larger Comptonized emission. By attributing the difference of the size of Compton cloud to the Alfvén radius, we can estimate the magnetic fields of neutron star. The obtained lower/upper limits are consistent with the previous results.

**Key words:** accretion, accretion disks — magnetic fields — stars: neutron — X-rays: binaries

---

## 1 Introduction

A neutron-star low-mass X-ray binary (NS-LMXB) consists of a weakly magnetized neutron star and a low-mass star. NS-LMXBs are known to exhibit soft and hard states in X-ray band, when their mass-accretion rate is high and low, respectively (e.g., Mitsuda et al. 1989; Matsuoka & Asai 2013). In the soft state, the spectra are dominated by a soft/thermal component, while a hard/Comptonized component is also recognized. The soft/thermal component is well described by an optically thick standard accretion disk model (Shakura & Sunyaev 1973). If the magnetic field of the NS is weak ( $\leq 10^8$  G), the magnetic field does not to affect the accretion flow, and the accretion disk can extend down to the NS surface. Most of the gas in the disk accretes onto the NS equatorial region. As the luminosity decreases, a soft-to-hard transition occurs in the inner disk from

optically thick to thin. Then the radius of the inner disk becomes larger. It is called a truncated disk (Done et al. 2007). The luminosity of soft-to-hard transition is known to be 1%–4% of the Eddington luminosity (Maccarone 2003). In the hard state, the spectra are dominated by a hard/Comptonized component, while a soft/thermal component is still required. The geometry of the accretion flow changes to the optically thin disk accreting to the whole surface of the NS.

The hard/Comptonized component has been observed in both soft and hard states (see Barret 2001 for a review). However, there are differences between the two states in the fitting parameters with the Comptonized component. In the soft state, the optical depth ( $\tau$ ) and the electron temperature ( $kT_e$ ) of the Comptonized component are  $\tau \sim 5\text{--}15$  and  $kT_e =$  a few keV, while those in the hard state are  $\tau \sim 2\text{--}3$  and  $kT_e =$  a few tens

of keV. Location of the Compton cloud has two possibilities. One is that the Compton cloud takes place in a transition layer (TL) (TL: Titarchuk et al. 1998) located between the disk and NS (e.g., Seifina & Titarchuk 2012; Titarchuk et al. 2013). The other is an accretion disk corona (ADC) above the disk (e.g., Church et al. 2014). Both the location of the Compton cloud and the origin of the seed photons remain uncertain. Furthermore, an additional hard X-ray component has been detected above  $\sim 30$  keV in the both states (e.g., Paizis et al. 2006). Origin of the emission also remains uncertain, although there are several models, such as Comptonization by bulk motion of accreting matter near the NS (e.g., Paizis et al. 2006), Comptonization by non-thermal electrons accelerated in a jet (e.g., Di Salvo et al. 2006), and synchrotron emission of energetic electrons (e.g., Markoff et al. 2001). Titarchuk, Seifina, and Shrader (2014) reported that the additional hard X-ray component was evidence for the presence a hot outer part of the TL (see also Seifina et al. 2015).

NS-LMXBs have been classified into two groups, Z sources and Atoll sources, based on their behavior on the color–color diagram and hardness–intensity diagram (Hasinger & van der Klis 1989). Z sources are bright and sometimes reach as close as the Eddington luminosity. On the other hand, Atoll sources are less bright, and some of them exhibit hard/soft spectral state transitions. In the color–color diagram, the distribution can be divided into two main regions, “banana” and “island.” The spectrum is usually softer in the banana than in the island. The distributions of the diagrams (of color–color and hardness–intensity) depend on the energy band, the instrument response, and the absorbing column density towards the source (Done & Gierliński 2003; Kuulkers et al. 1994). Gladstone, Done, and Gierliński (2007) investigated how the banana branch moves in the color–color diagram (soft color: 4–6.4 keV/3–4 keV and hard color: 9.7–16 keV/6.4–9.7 keV) for inclination angles of  $30^\circ$ ,  $60^\circ$ , and  $70^\circ$ . The change is mainly in the soft color. They also investigated the effect of  $kT_e$  of 2.5, 3.0, and 3.5 keV for each inclination angle. This matches very well with the location and the shape of the banana branches in their color–color diagrams.

The surface magnetic field of the NS is believed to be higher in the Z sources ( $\sim 10^9$  G) than in the Atoll sources ( $\sim 10^8$  G) (Zhang & Kojima 2006). For example, the magnetic field of a Z-source Cyg X-2 was estimated to be  $2.2 \times 10^9$  G from the observed oscillations in the horizontal-branch and the beat frequency model (Focke 1996). For a transient Z-source XTE J1701–462, the magnetic field was estimated to be  $\sim (1-3) \times 10^9$  G from the interaction between the magnetosphere and the radiation-pressure-dominated accretion disk (Ding et al. 2011). Meanwhile, two Atoll sources, 4U 1608–52 and Aql X-1, were estimated to have magnetic fields of  $10^7$ – $10^8$  G from the propeller effect (4U 1608–52: Chen et al. 2006; Asai et al. 2013, Aql X-1: Campana et al. 1998; Zhang et al. 1998; Asai

et al. 2013). However, Titarchuk, Bradshaw, and Wood (2001) suggested that both Z sources and Atoll sources have a very low surface magnetic fields of  $\sim 10^7$ – $10^8$  G based on their magneto-acoustic wave model and the observed kHz QPOs. Also using the kHz QPO, Campana (2000) estimated the magnetic field of  $\sim (1-8) \times 10^8$  G for Cyg X-2 from the kHz QPO observability in the variations of the NS magnetosphere radius (Alfvén radius). Campana (2000) also reported that the magnetic fields of two Atoll sources, 4U 1820–30 and Aql X-1 were estimated to be  $\sim 2 \times 10^8$  G and  $\sim (0.3-1) \times 10^8$  G, respectively.

In general, the effect of the magnetic fields of NS-LMXB is ignored because it is weak. However, in some cases, importance of the effect is suggested (e.g., Campana 2000; Cui et al. 1998; Ding et al. 2011; Wang et al. 2011). Ding et al. (2011) suggested that the inner disk radius could be set by the magnetospheric radius when the gas pressure from disk decreases by large radiation pressure and the magnetosphere expands. Wang et al. (2011) considered a TL between the innermost Keplerian orbit and the magnetosphere, and suggested that the accretion flow is disturbed by the several instabilities. Furthermore, Campana (2000) suggested that the disappearance of the kHz QPO was related to the disappearance of magnetosphere (see also Cui et al. 1998). They also noted that the effect of magnetic field of NS must be taken into account. In this study, we considered the effect of the magnetic fields of NS.

We investigated average hardness ratio ( $HR$ : 15–50 keV/2–10 keV) in the soft state of nine bright Atoll NS-LMXBs using MAXI (Matsuoka et al. 2009)/GSC (Gas Slit Camera: Mihara et al. 2011; Sugizaki et al. 2011)<sup>1</sup> and Swift (Gehrels et al. 2004)/BAT (Burst Alert Telescope: Barthelmy et al. 2005)<sup>2</sup> from 2009 August 15 (MJD = 55058) to 2015 August 15 (MJD = 57249). In section 2, we describe the data selection and analysis of the hardness–luminosity diagram. In section 3, we discuss the relation between hard tail emission and magnetic fields of NS-LMXB. The conclusion is presented in section 4.

## 2 Analysis and results

### 2.1 Distribution of hardness ratio (15–50 keV/2–10 keV)

We obtained long-term one-day bin light curves of MAXI/GSC and Swift/BAT for nine bright Atoll NS-LMXBs. The light curves of 2–10 keV band of GSC and 15–50 keV band of BAT and the  $HR$  of the two bands are shown for each source in figure 1–3. The obtained count rates of GSC and BAT were converted to luminosities by assuming a Crab-like spectrum (Kirsch et al. 2005) and the distances listed in table 1. The assumption of Crab-like spectrum is acceptable in the hard state, because the energy spectrum is dominated by the Comptonized

<sup>1</sup> <<http://maxi.riken.jp/>>.

<sup>2</sup> <<http://heasarc.gsfc.nasa.gov/docs/swift/results/transients/>>.

emission approximated by a power law with the photon index of 1–2. On the other hand, in the soft state, the energy spectrum is dominated by the thermal emission. The obtained luminosity by assuming Crab-like spectrum is underestimated in the 2–10 keV band, but is overestimated in the 15–50 keV band. As a result, the  $HR$  of two energy bands is overestimated by 2.0 times (see Asai et al. 2015 for detail). Therefore, we handle only the relative difference (see appendix).

Figure 4 shows the histograms (number of days) of the  $HR$  (BAT/GSC) of all the nine NS-LMXBs. The peak around  $HR=1$  corresponds to the hard state, while the distribution around  $HR=0.1$  corresponds to the soft state. The soft state shows two peaks. The boundary of the two peaks ( $HR$  at the smallest value) is 0.09 (dotted line in figure 4). We also make the distributions of  $HR$ s for the individual sources in figure 5. The distributions of the soft state are divided into two groups using the peak value of  $HR$ . One is that  $HR$  of the peak is smaller than 0.09: Aql X-1, 4U 1608–52, GX 3+1, GX 9+9, GX 13+1, and GX 9+1. The other is that the  $HR$  is larger than 0.09: 4U 1820–30 and 4U 1735–44. We note that 4U 1705–44 is exceptional since the peak is at  $HR=0.09$ .

## 2.2 Hardness–luminosity diagram

To investigate the difference between two groups in the soft state, we selected the data of only the soft state. Table 1 shows periods of the soft state that are analyzed in this paper. Four sources (GX 3+1, GX 9+9, GX 13+1, and GX 9+1) stayed in the soft state during the observed period, which is obvious since there is no distribution of the hard state (around  $HR=1$ ) in figure 5. In contrast to the four sources, other five sources show both the soft and hard states. The individual selection of the soft state is summarized as follows.

**Aql X-1:** The source stayed in the soft state during five outbursts (see figure 1). The  $HR$  threshold between the soft and hard states was chosen 0.222 in one-day bin data, which is taken after the analysis in Asai et al. (2015). When the state transition continues for more than one day, we excluded the data and used the data only in a stable  $HR$ .

**4U 1608–52:** The source stayed in soft state during six outbursts and mini-outbursts during MJD = 55900–56100 (see figure 1). The  $HR$  threshold was chosen 0.224 in one-day bin data after Asai et al. (2015). We excluded the data during the transition in the same way as Aql X-1. We also removed the data of mini-outbursts, because the spectral states repeated between the soft and hard states in short durations (less than several tens of days).

**4U 1705–44:** The source stays in soft state during three outbursts and mini-outbursts during MJD = 55058–55400 and 55800–56100 (see figure 1). The  $HR$  threshold

was chosen 0.355 in one-day bin data after Asai et al. (2015). We excluded the data during the transition in the same way as Aql X-1, and the data of mini-outbursts as 4U 1608–52.

**4U 1820–30:** Although 4U 1820–30 stays in the soft states in most of the time, it became the hard state ( $HR > 0.2$ : Asai et al. 2015) eight times (see figure 3). We excluded the data in the eight hard states.

**4U 1735–44:** Although 4U 1735–44 stays in the soft states in most of the time, it became the hard state ( $HR \sim 1$ ) only once (see figure 3). We excluded the data in the hard state.

Figure 6 shows hardness–luminosity diagrams during the soft state for each source. The gray backdrop is the distribution of all the nine sources. The vertical dotted lines represent the threshold that we determined in figure 4. The nine sources are divided into two groups except for 4U 1705–44. One is distributed in the lower part than the threshold of 0.09 (Aql X-1, 4U 1608–52, GX 3+1, GX 9+9, GX 13+1, and GX 9+1). The other is distributed in the higher part than the threshold (4U 1820–30 and 4U 1735–44).

After excluding 4U 1705–44, both figure 5 and figure 6 show that eight NS-LMXBs are divided into two groups by the threshold of  $HR = 0.09$ . This result is consistent with the results of spectral model fitting for RXTE data of 4U 1820–30 and GX 3+1 (see Appendix). In the next section, we discuss the difference of  $HR$ .

## 3 Discussion

We investigated average hard-tail X-ray emission in the soft state of nine bright Atoll NS-LMXBs, where the magnitude of the hard tail is defined by  $HR$  (15–50/2–10 keV, see figure 4 and 5). We can classify the  $HR$  into at least two groups; larger hard tail (4U 1820–30 and 4U 1735–44) and smaller hard tail (Aql X-1, 4U 1608–52, GX 3+1, GX 9+9, GX 13+1, and GX 9+1) (see figures 6 and 10). In this section, we give a reasonable phenomenological interpretation of the observational results. The results would be related to properties of each NS, such as magnetic fields.

### 3.1 Differences of inclination, electron temperature, and seed photon

The difference of  $HR$  (15–50/2–10 keV) comes from that of the 15–50 keV luminosity, because the  $HR$  is almost constant for a wide range of 2–10 keV luminosity. For example, the 2–10 keV luminosities of both sources, Aql X-1 and 4U 1820–30, are in the same range of  $(\sim 1.2\text{--}30) \times 10^{36}$  erg s<sup>-1</sup>. On the other hand, the  $HR$  of Aql X-1 is smaller than 0.09 and that of 4U 1820–30 is larger than 0.09 as shown in figure 6. The

emission in the 15–50 keV energy band is known to originate from the Comptonized component.

We show the  $HR$  of the energy range (15–50/2–10 keV) would not be affected by the following differences as below.

**Inclination** In general, the difference in the  $HR$  distribution is interpreted by the difference of the inclination of the system (Gladstone et al. 2007). When the inclination is high,  $HR$  tend to be large because of large  $\tau$ . GX 13+1 is known to be high inclination system because of the periodic dipping and the deep Fe absorption features (60–80°; Díaz Trigo et al. 2012; D’Ài et al. 2014). If the distribution of  $HR$  in figure 6 reflects the inclination, GX 13+1 is expected to distribute in the higher part than the threshold (0.09). However, the result is opposite. The other sources would not be high inclination system because periodic dipping has not been reported. Thus the value of  $HR$  would be independent of the inclination, when we used the energy band of 15–50/2–10 keV.

**Electron temperature  $kT_e$  of Compton cloud** In the soft state,  $kT_e$  is typically a few keV (see Barret 2001 for a review). The difference in the  $HR$  distribution is interpreted by the difference of  $kT_e$  of the Compton cloud (Gladstone et al. 2007). When  $kT_e$  is high,  $HR$  tend to be large because Compton-up scattering occurs up to high energy. Titarchuk, Seifina, and Frontera (2013) reported that  $kT_e$  changes from 2.9 keV to 6 keV for upper banana in both 4U 1820–30 and GX 3+1. If the distribution of  $HR$  in figure 6 reflected  $kT_e$ , the distributions of  $HR$  in both 4U 1820–30 and GX 3+1 are expected to be the same. However, the distributions of the two sources are not the same and are divided into the top and bottom of the threshold (0.09). The change of  $kT_e$  as described by Titarchuk, Seifina, and Frontera (2013) would appear as the scatter in the  $HR$  for each source.

The  $HR$  of 4U 1820–30 and 4U 1735–44 is larger than the threshold. In the case of 4U 1820–30, the composition of the accreting matter is helium (Rappaport et al. 1987).  $kT_e$  would be higher than hydrogen accretion of other sources. However, the orbital period (thus separation) of 4U 1735–44 is large and the companion star would be a normal star. Thus the accreting matter would be hydrogen. Helium accretion cannot be a common reason for the large Compton component. Thus, the classification of two groups of  $HR$  is independent of  $kT_e$ .

#### Origin of the seed photon to Compton cloud

The Comptonized component is also characterized by the seed photon. The seed photons is considered to be soft photons from NS surface and/or disk photons in soft state (e.g., Sakurai et al. 2012; Seifina & Titarchuk 2012; Titarchuk et al. 2013). The difference would

not affect the distribution of  $HR$ , because the  $HR$  is almost constant over the large range of luminosity of  $(7–50) \times 10^{36}$  erg s<sup>-1</sup>.

Therefore, we propose that the difference between two groups would be due to the size<sup>3</sup> of the Compton cloud. The group with a larger  $HR$  than 0.09 (4U 1820–30 and 4U 1735–44) would have larger Compton cloud than another group with a smaller  $HR$  than 0.09. We notice that the  $HR$  of 4U 1705–44 indicates an intermediate value between two groups.

### 3.2 Location of Compton cloud

In the soft state, Comptonized emission is considered to be formed in the TL located between the accretion disk and NS surface (e.g., Seifina & Titarchuk 2012; Titarchuk et al. 2013) and/or in the ADC above the accretion disk (e.g., Church et al. 2014). Although the location is controversial, the size of Compton cloud would change with the amount of accretion flow. However, there is no correlation between the observed luminosity and the  $HR$  between the two groups. Here, let us take into account of the magnetic field of the NS. Although the magnetic field of NS in NS-LMXB is considered to be weak, in some cases the effect of the magnetic field is taken into account (e.g., Campana 2000; Cui et al. 1998; Ding et al. 2011; Wang et al. 2011). In the soft state, most of the gas in the disk accretes onto the NS equatorial region, because the disk can extend to the NS surface or the innermost stable circular orbit (ISCO). The accretion flow is thermalized on the NS surface, and the emission from there is Comptonized by the plasma around NS. However, if the magnetic field of the NS is  $\geq 10^8$  G, the Alfvén radius would be larger than the ISCO/NS surface. In this case, the accretion disk would be terminated at the Alfvén radius. The similar situation is suggested by Ding et al. (2011), although they considered the radiation-pressure-dominated accretion disk. Then the accretion flow spreading vertically at the Alfvén radius would create relatively large Compton cloud. In the TL model, the outer boundary of the TL corresponds to the Alfvén radius. The difference between  $HR$ s is reflected on whether the Alfvén radius is larger than ISCO/NS surface.

Alfvén radius is the radius at which the gas pressure is equal to the magnetic pressure of the magnetosphere. It depends on both the mass of the accretion flow and the magnetic field of the NS. Using the Alfvén radius ( $R_{A0}$ ) in a spherically symmetric mass flow, the general Alfvén radius ( $R_A$ ) is expressed as the following equation (Ghosh & Lamb 1979; Matsuoka & Asai 2013):

<sup>3</sup> Correctly speaking, the “size” is optical depth  $\times$  solid angle from the photon source of the Compton cloud. If the optical depth is similar, the difference of the solid angle is reflected. When the distance between the photon source and the Compton cloud is similar, the solid angle is the proportional to the size of the Compton cloud. We use the word “size” in this context.

$$R_A = \eta R_{A0} = 3.7 \times 10^6 \eta (L/10^{36} \text{ erg s}^{-1})^{-2/7} (B/10^8 \text{ G})^{4/7} \\ \times (M_{\text{NS}}/1.4M_{\odot})^{1/7} (R_{\text{NS}}/10^6 \text{ cm})^{10/7} \text{ cm, (1)}$$

where  $G$ ,  $B$ ,  $M_{\text{NS}}$ ,  $R_{\text{NS}}$ , and  $M_{\odot}$  are the gravitational constant, the magnetic field of the NS pole, the mass of the NS, the radius of the NS, and solar mass, respectively. The original expression (27) of Ghosh and Lamb (1979) is changed by substituting  $\mu = BR_{\text{NS}}^3$  and  $dM/dt = LR_{\text{NS}}/GM$  for the equation of the magnetic dipole moment of the NS and the relation between the mass accretion rate  $dM/dt$  and the total luminosity  $L$ , respectively. The factor  $\eta$  is expressed as a value of  $\sim 0.52$ – $1$  depending on the model and the effect of the mass accretion flow. Approximately,  $\eta \sim 0.52$  corresponds to a disk-like accretion flow and  $\eta \sim 1$  corresponds to a spherical accretion flow<sup>4</sup>.

We calculated  $R_A$  as a function of  $L$  when  $B$  is from  $0.5 \times 10^8 \text{ G}$  to  $3.5 \times 10^8 \text{ G}$ , as shown in figure 7. We adopted  $\eta = 0.52$  because the accretion flow is considered to be a disk-like accretion flow in the soft state. We also adopted  $M_{\text{NS}} = 1.4M_{\odot}$  and  $R_{\text{NS}} = 10^6 \text{ cm}$ . We also plotted the radius of ISCO and NS. ISCO is  $3r_g$ , where  $r_g$  is the Schwarzschild radius ( $=2GM/c^2$ ). Here, ISCO is  $1.2 \times 10^6 \text{ cm}$  for  $M_{\text{NS}} = 1.4M_{\odot}$ . When  $L$  is  $10^{37} \text{ erg s}^{-1}$ ,  $R_A$  is larger than ISCO for  $B > 1.5 \times 10^8 \text{ G}$ . In this case, the accretion flow would be stopped and spread at the Alfvén radius, and then the relatively large Compton cloud would be created. As a result, the  $HR$  would be large (for example  $HR > 0.09$ ). On the other hand, when  $B < 1 \times 10^8 \text{ G}$ , the  $R_A$  is smaller than both ISCO and NS surface. In this case, the accretion flow is not affected by the magnetic field, and then most of the gas in the disk accretes onto the NS equatorial region. The  $HR$  would be low (for example  $HR < 0.09$ ).

Figure 8 illustrates the schematic drawings of suggesting geometry of NS-LMXB in a soft state. Assuming  $M_{\text{NS}} = 1.4M_{\odot}$  and  $B = 2 \times 10^8 \text{ G}$ , (a)  $R_A = 1.2 \times 10^6 \text{ cm}$ , (b)  $R_A = 1.3 \times 10^6 \text{ cm}$ , and (c)  $R_A = 1.5 \times 10^6 \text{ cm}$  for  $L = 20 \times 10^{36} \text{ erg s}^{-1}$ ,  $15 \times 10^{36} \text{ erg s}^{-1}$ , and  $10 \times 10^{36} \text{ erg s}^{-1}$ , respectively. According to increasing the luminosity,  $R_A$  becomes smaller and the size of Compton cloud would be smaller. However, the solid angle from the photon source is constant. Thus,  $HR$  is constant even if the luminosity is increasing as long as  $R_A$  is larger than the ISCO (figure 8b and 8c).

Here, we define the threshold luminosity ( $L_{\text{th}}$ ) where the  $R_A$  equals the ISCO in equation (1). In this figure,  $L_{\text{th}} = 20 \times 10^{36} \text{ erg s}^{-1}$ . When the luminosity is higher than  $L_{\text{th}}$ ,  $R_A$  is smaller than ISCO and  $HR$  is below 0.09 (figure 8a). On the other hand, when the luminosity is lower than  $L_{\text{th}}$ ,  $R_A$  is larger than ISCO and  $HR$  is above 0.09 (figure 8b and 8c).

<sup>4</sup> We notice that Wang (1997) estimated  $\eta \sim 1$  even in the case of disk-like accretion flow. They calculated torque in inclined magnetic moment axis to the spin axis assuming that the spin axis was normal to the disk plane.

### 3.3 Magnetic field derived from the threshold luminosity

Next, we try to estimate the magnetic field ( $B$ ) of the NS using the difference of the  $HR$ . We defined  $L_{\text{th}}$  in previous subsection. Here, we use the ISCO rather than the NS surface, since the ISCO is  $1.2 \times 10^6 \text{ cm}$  which is larger than the  $R_{\text{NS}}$ , employing traditional values of  $R_{\text{NS}} = 1 \times 10^6 \text{ cm}$  and  $M_{\text{NS}} = 1.4M_{\odot}$ . We note that the ISCO is not always larger than the  $R_{\text{NS}}$  (e.g., Wang et al. 2015). Since uncertainty remains for both the radius and mass, we adopt the traditional values. If the luminosity is higher than  $L_{\text{th}}$ ,  $R_A$  is smaller than the ISCO. In this case, the accretion disk would not be affected by the magnetic field and the large Compton cloud would not be created. The  $HR$  remains small ( $< 0.09$ ). When the observed  $HR$  is always smaller than 0.09 in one source, the minimum observed luminosity becomes the upper limit of  $L_{\text{th}}$ . On the other hand, when the observed  $HR$  is always larger than 0.09, the maximum observed luminosity becomes the lower limit of  $L_{\text{th}}$ . Thus, we can estimate the upper/lower limits of  $B$  from the upper/lower limits of  $L_{\text{th}}$ .

First, we determined  $L_{\text{th}}$  from the hardness–luminosity diagrams (figure 6). The value  $L_{\text{th}}$  are listed in table 2. Here, for 4U 1705–44, we adopted the lower-end luminosity of the distribution on  $HR = 0.09$  as  $L_{\text{th}}$ , because the  $HR$  of 4U 1705–44 distribute around  $HR = 0.09$ . This means that the luminosity change over  $L_{\text{th}}$ . Substituting  $R_A = \text{ISCO}$  of  $1.2 \times 10^6 \text{ cm}$  and  $L = L_{\text{th}}$  in the quotation (1), we obtained  $B$  as in table 2. The values  $B$  of Aql X-1 and 4U 1608–52 are consistent with those reported previously. Although the  $B$  of 4U 1820–30 ( $> 3.2 \times 10^8 \text{ G}$ ) is somewhat larger than the reported value of  $\sim 2 \times 10^8 \text{ G}$  (Campana 2000), our values are consistent in the sense that the  $B$  of 4U 1820–30 is larger than those of Aql X-1 and 4U 1608–52.

Next, we plotted the hardness–“normalized luminosity” diagram for all the sources in figure 9b. The luminosities of figure 6 were normalized by the  $L_{\text{th}}$ . Figure 9a shows the hardness–luminosity diagram for all the sources to realize the effect of the normalization. After the normalization, in figure 9b, the data points are distributed on a single trend from upper-left to lower-right. The data points in the upper-left section can be interpreted as the accretion flow is spread vertically at  $R_A$ . Meanwhile, the data points in the lower-right section can be interpreted as the accretion flow is not affected by the magnetic fields. We also presented the hardness–“normalized luminosity” diagrams for individual sources in figure 10.

According to the fact that the frequency of the upper kHz QPO is related to the Keplerian frequency at the inner edge of an accretion disk, Campana (2000) suggested that the disappearance of kHz QPO at high luminosities may be related to the disappearance of the magnetosphere at the time when  $R_A$  reaches  $R_{\text{NS}}$ . Then we can assume that the disappearance of the kHz QPO is related to a smaller  $HR$  ( $< 0.09$ ) in our sources.

In table 2 we listed in existence of reported kHz QPO (van der Klis 2006). The kHz QPO was observed from large  $HR$  ( $\geq 0.09$ ) sources (4U 1705–44, 4U 1820–30, and 4U 1735–44) while it was not observed from small  $HR$  ( $\leq 0.09$ ) sources (GX 3+1, GX 9+9, GX 13+1, and GX 9+1). In the cases of Aql X-1 and 4U 1608–52, the kHz QPO was detected even though they have small  $HR$ . For Aql X-1, Campana (2000) reported that the kHz QPO disappeared at the luminosity (2–10 keV) higher than  $3.6 \times 10^{36}$  erg s<sup>-1</sup>. Similarly, for 4U 1608–52, the kHz QPOs were detected only when the luminosity (2–20 keV) dropped down to  $10^{37}$  erg s<sup>-1</sup> (Méndez et al. 1998). Namely, the kHz QPO was not detected in the soft state ( $> 10^{37}$  erg s<sup>-1</sup>). Therefore, the existence/absence of the kHz QPO is consistent with our results of the large/small  $HR$ .

## 4 Conclusion

We investigated average hard-tail X-ray emission in the soft state of nine bright Atoll NS-LMXBs by using the light curves of MAXI/GSC and Swift/BAT, and tried to relate the difference of  $HR$ s to that of  $B$  of NSs. When  $R_A$  is larger than the ISCO, the accretion disk would be stopped and spread at  $R_A$ , and then the relatively large Compton cloud would be created. Then, the  $HR$  would become large ( $> 0.09$ ), and the observed luminosity is lower than the  $L_{th}$ , where the  $L_{th}$  is the luminosity at which the  $R_A$  equals the ISCO. We can drive the lower limit of  $B$  of the NS from the lower limits of  $L_{th}$ . Since  $HR$  of 4U 1820–30 and 4U 1735–44 is large,  $B_s$  is estimated as  $B_s \gtrsim 2.5 \times 10^8$  G. The upper limit of  $B$  is given for other seven sources. These results are consistent with the previous results.

## Acknowledgments

We would like to acknowledge the MAXI team for MAXI operation and for analyzing real-time data.

## Appendix. Hardness–intensity diagram

Here we investigate the validity of assuming a Crab-like spectrum for a soft state in the conversion from the count rate of GSC and BAT to the luminosity (see subsection 2.1). In a soft state, the luminosity obtained in this way is underestimated in the 2–10 keV, but is overestimated in the 15–50 keV. Therefore, we handle only the relative difference of  $HR$ . Here we compare  $HR$  obtained by assuming a Crab-like spectrum with that obtained by spectral model fitting for RXTE data. The latter was taken from table 4 of Titarchuk, Seifina, and Frontera (2013) for 4U 1820–30 and table 4 of Seifina and Titarchuk (2012) for GX 3+1. Figure 11 shows the hardness–luminosity diagram in both cases. The data of 4U 1820–30 included those of the soft and hard state in both cases. The energy band of  $HR$  is slightly different. The  $HR$  of figure 11a is 15–50 keV/2–10 keV. In fig-

ure 11b, the  $HR$  of 4U 1820–30 and GX 3+1 is 10–50 keV/3–10 keV and 10–60 keV/3–10 keV, respectively. In spite of the difference of energy band, the  $HR$  of 4U 1820–30 is larger than that of GX 3+1 in both figure 11a and 11b. Thus, relative difference of  $HR$  assuming a Crab-like spectrum is consistent with the result of spectral model fitting.

## References

- Asai, K., et al. 2013, *ApJ*, 773, 117  
 Asai, K., Mihara, T., Matsuoka, M., & Sugizaki, M. 2015, *PASJ*, 67, 92  
 Barret, D. 2001, *Advances in Space Research*, 28, 307  
 Barthelmy, S. D., et al. 2005, *Space Sci. Rev.*, 120, 143  
 Campana, S. 2000, *ApJ*, 534, L79  
 Campana, S., Stella, L., Mereghetti, S., Colpi, M., Tavani, M., Ricci, D., Dal Fiume, D., & Belloni, T. 1998, *ApJ*, 499, L65  
 Chen, X., Zhang, S. N., & Ding, G. Q. 2006, *ApJ*, 650, 299  
 Christian, D. J., & Swank, J. H. 1997, *ApJS*, 109, 177  
 Church, M. J., Gibiec, A., & Bałucińska-Church, M. 2014, *MNRAS*, 438, 2784  
 Cui, W., Barret, D., Zhang, S. N., Chen, W., Boirin, L., Swank, J. 1998, *ApJ*, 502, L49  
 D’Ai, A., Iaria, R., Di Salvo, T., Riggio, A., Burderi, L., & Robba, N. R. 2014, *A&A*, 564, A62  
 Díaz Trigo, M., Sidoli, L., Boirin, L., & Parmar, A. N. 2012, *A&A*, 543, A50  
 Di Salvo, T., et al. 2006, *ApJL*, 649, L91  
 Ding, G. Q., Zhang, S. N., Wang, N., Qu, J. L., & Yan, S. P. 2011, *AJ*, 142, 34  
 Done, C., & Gierliński, M. 2003, *MNRAS*, 342, 1041  
 Done, C., Gierliński, M., & Kubota, A. 2007, *A&AR*, 15, 1  
 Focke, W. B. 1996, *ApJL*, 470, L127  
 Galloway, D. K., Muno, M. P., Hartman, J. M., Psaltis, D., & Chakrabarty, D. 2008, *ApJS*, 179, 360  
 Gehrels, N., et al. 2004, *ApJ*, 611, 1005  
 Ghosh, P., & Lamb, F. K. 1979, *ApJ*, 232, 259  
 Gladstone, J., Done, C., & Gierliński, M. 2007, *MNRAS*, 378, 13  
 Hasinger, G. & van der Klis, M. 1989, *A&A*, 225, 79  
 Kirsch, M. G., et al. 2005, *Proc. SPIE*, 5898, 22  
 Kuulkers, E., & van der Klis, M. 2000, *A&A*, 356, L45  
 Kuulkers, E., van der Klis, M., Oosterbroek, T., Asai, K., Dotani, T., van Paradijs, J., & Lewin, W. H. G. 1994, *A&A*, 289, 795  
 Liu, Q. Z., van Paradijs, J., & van den Heuvel, E. P. J. 2007, *A&A*, 469, 807  
 Maccarone, T. J. 2003, *A&A*, 409, 697  
 Markoff, S., Falcke, H., & Fender, R. 2001, *A&A*, 372, L25  
 Matsuoka, M., et al. 2009, *PASJ*, 61, 999  
 Matsuoka, M., & Asai, K. 2013, *PASJ*, 65, 26  
 Méndez, M., van der Klis, M., Wijnands, R., Ford, E. C., van Paradijs, J., & Vaughan, B. A. 1998, *ApJL*, 505, L23  
 Mihara, T., et al. 2011, *PASJ*, 63, S623  
 Mitsuda, K., Inoue, H., Nakamura, N., & Tanaka, Y. 1989, *PASJ*, 41, 97  
 Paizis, A., et al. 2006, *A&A*, 459, 187  
 Rappaport, S., Ma, C. P., Joss, P. C., & Nelson, L. A. 1987, *ApJ*, 322, 842  
 Sakurai, S., Yamada, S., Torii, S., Noda, H., Nakazawa, K., Makishima, K., & Takahashi, H. 2012, *PASJ*, 64, 72  
 Shakura, N. I., & Sunyaev, R. A. 1973, *A&A*, 24, 337

- 
- Seifina, E., & Titarchuk, L. 2012, *ApJ*, 747, 99
- Seifina, E., Titarchuk, L., Shrader, C., & Shaposhnikov, N. 2015, *ApJ*, 808, 142
- Sugizaki, M., et al. 2011, *PASJ*, 63, S635
- Titarchuk, L. G., Bradshaw, C. F., & Wood, K. S. 2001, *ApJL*, 560, L55
- Titarchuk, L., Lapidus, I., & Muslimov, A. 1998, *ApJ*, 499, 315
- Titarchuk, L., Seifina, E., & Frontera, F. 2013, *ApJ*, 767, 160
- Titarchuk, L., Seifina, E., & Shrader, C. 2014, *ApJ*, 789, 98
- van der Klis, M. 2006, *Compact stellar X-ray sources*, 39
- Wang, Y.-M. 1997, *ApJ*, 475, L135
- Wang, D. H., Chen, L., Zhang, C. M., Lei, Y. J., Qu, J. L., & Song, L. M. 2015, *MNRAS*, 454, 1231
- Wang, J., Zhang, C. M., Zhao, Y. H., Lin, Y. F., Yin, H. X. & Song, L. M. 2011, *A&A*, 528, A126
- Zhang, C. M., & Kojima, Y. 2006, *MNRAS*, 366, 137
- Zhang, S. N., Yu, W., & Zhang, W. 1998, *ApJL*, 494, L71

**Table 1.** Periods of the soft states defined by MAXI/GSC and Swift/BAT, and distance used in this paper.

Name	Period of soft states (MJD)	Distance (kpc)	Ref.*
Aql X-1	55157–55170, 55451–55479, 55857–55899, 56460–56513, 56853–56873	5	(1)
4U1608–52	55260–55272, 55645–55721, 56213–56226, 56442–56445, 56673–56734, 56937–56945	4.1	(2)
4U1705–44	55410–55684, 55717–55915, 56048–57249	7.4	(1)
GX 3+1	55058–57249	4.5	(4)
GX 9+9	55058–57249	5	(3)
GX 13+1	55058–57249	7	(1)
GX 9+1	55058–57249	5	(1)
4U 1820–30	55058–55288, 55306–55615, 55629–56130, 56141–56474, 56482–56619, 56681–56986 56995–57132, 57145–57151, 57167–57249	7.6	(1)
4U 1735–44	55058–56766, 56775–57249	8.5	(2)

\* (1) Liu et al. (2007), (2) Galloway et al. (2008), (3) Christian and Swank (1997), and (4) Kuulkers and van der Klis (2000).

**Table 2.** Threshold luminosity and corresponding magnetic fields.

Name	HR of peak	$L_{\text{th}}^*$ $10^{36} \text{ erg s}^{-1}$	$B$ $10^8 \text{ G}$	kHz QPO <sup>†</sup>	Reported $B$ $10^8 \text{ G}$	Ref. <sup>‡</sup>
Aql X-1	< 0.09	$\lesssim 11$	$\lesssim 1.4$	○	0.3–1.9	(1), (2), (3), (4)
4U1608–52	< 0.09	$\sim 8$	$\sim 1.2$	○	0.5–1.6	(4), (5)
4U1705–44	= 0.09	$\sim 20$	$\sim 1.9$	○	–	–
GX 3+1	< 0.09	$\sim 8$	$\sim 1.2$	–	–	–
GX 9+9	< 0.09	$\sim 9$	$\sim 1.3$	–	–	–
GX 13+1	< 0.09	$\sim 30$	$\sim 2.4$	–	–	–
GX 9+1	< 0.09	$\sim 23$	$\sim 2.1$	–	–	–
4U1820–30	> 0.09	$\gtrsim 55$	$\gtrsim 3.2$	●	$\sim 2$	(3)
4U1735–44	> 0.09	$\gtrsim 34$	$\gtrsim 2.5$	●	–	–

\* Threshold luminosity in the 2–10 keV band (see text for explanation).

† ●: kHz QPOs have been reported in soft state. ○: kHz QPOs have been reported, although the state is not clear. –: not reported (van der Klis 2006).

‡ (1) propeller effect (Campana et al. 1998), (2) propeller effect (Zhang et al. 1998), (3) kHz QPO (Campana 2000), (4) propeller effect (Asai et al. 2013), and (5) propeller effect (Chen et al. 2006).



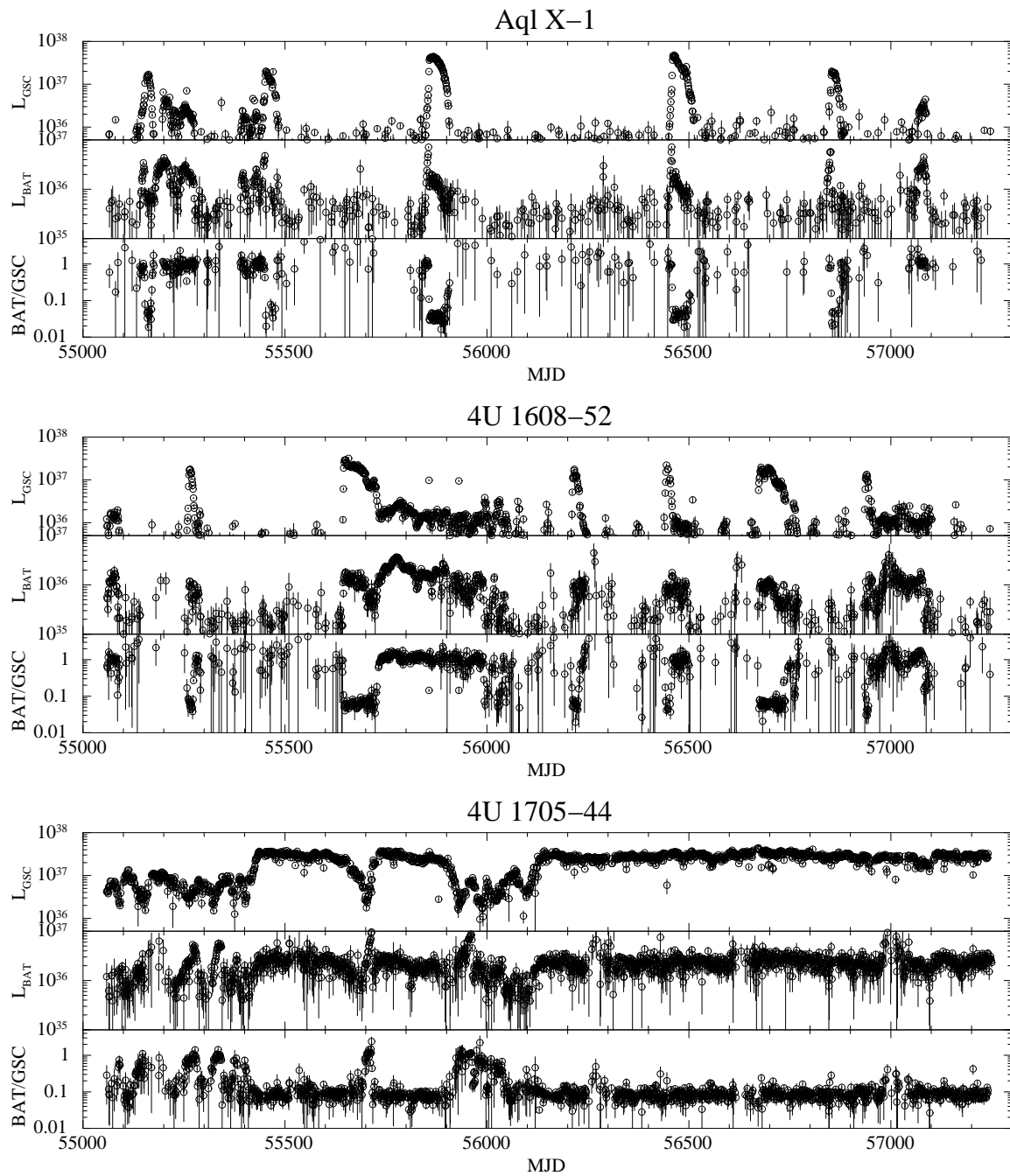
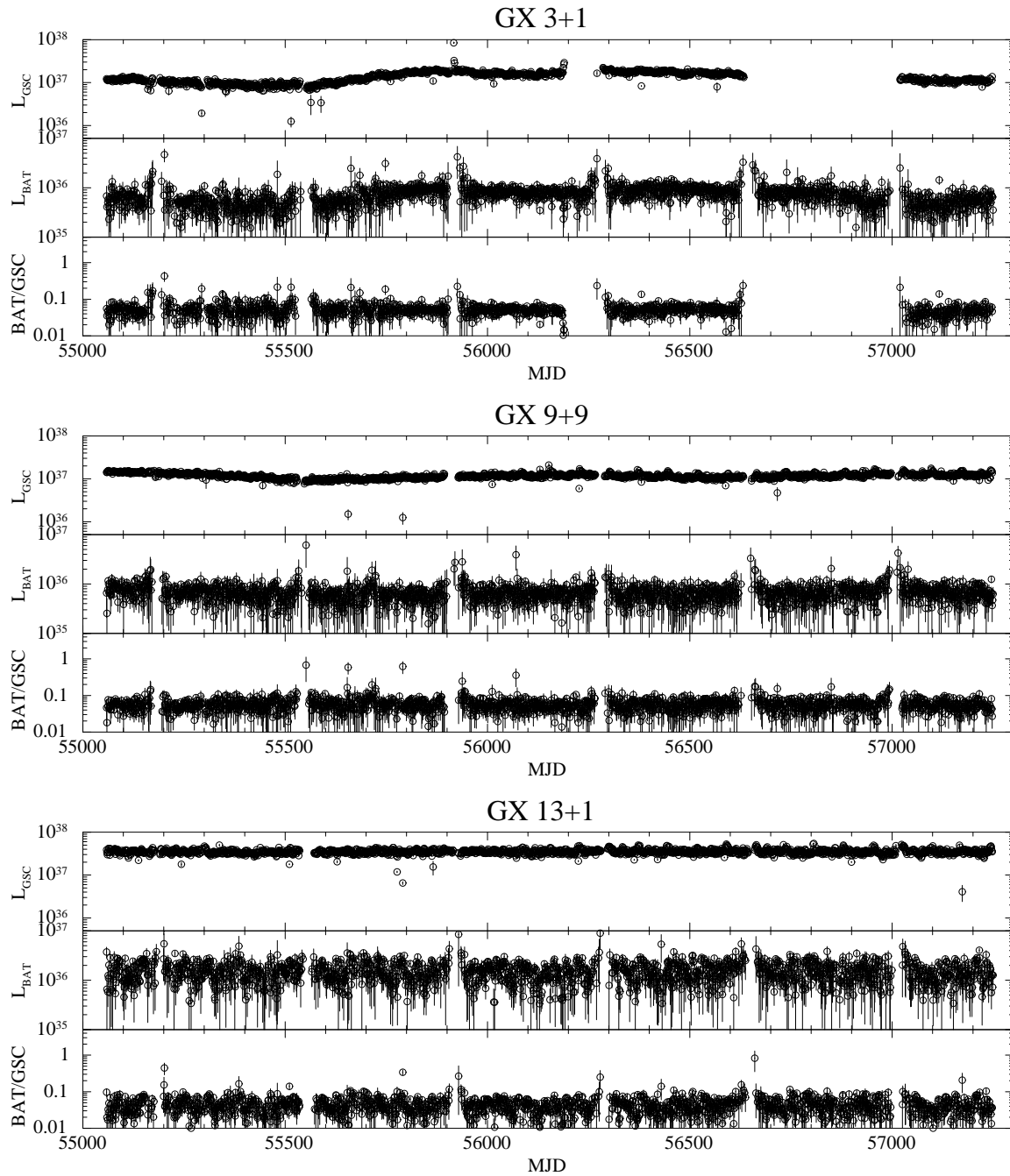


Fig. 1. One-day GSC light curves in the 2–10 keV band, one-day BAT light curves in the 15–50 keV band, and the hardness ratio (BAT/GSC) of Aql X-1, 4U 1608–52, and 4U 1705–44.  $L_{\text{GSC}}$  and  $L_{\text{BAT}}$  are the luminosities in units of erg s $^{-1}$ . Vertical error bars represent 1- $\sigma$  statistical uncertainty.



**Fig. 2.** Same as figure 1, but for GX 3+1, GX 9+9, and GX 13+1. One-year periodic rises before and after data gaps in the Swift/BAT light curves are due to instrumental effect. MAXI/GSC data gaps in GX 3+1 in MJD=56187–56287 and 56652–56997 are due to contamination source.

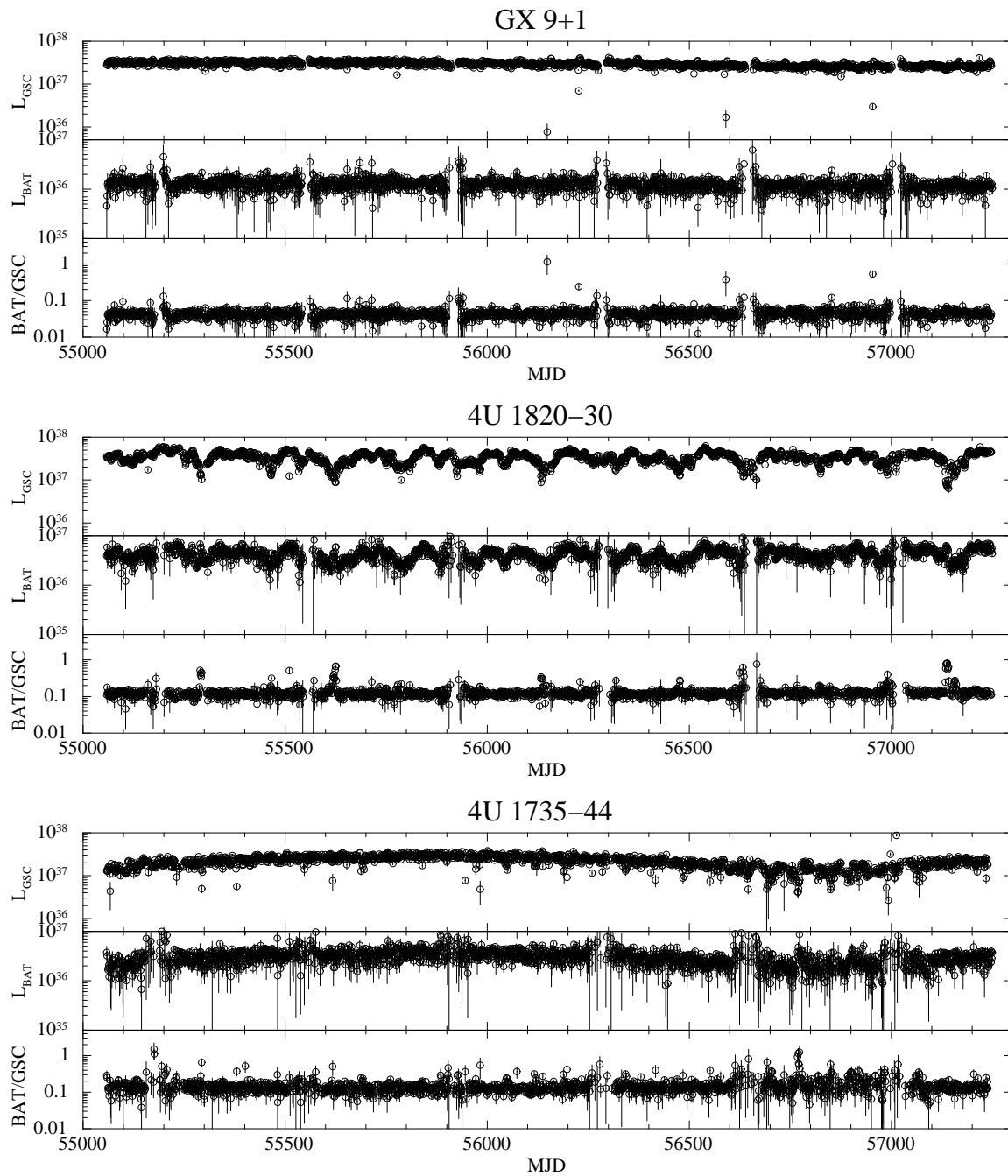
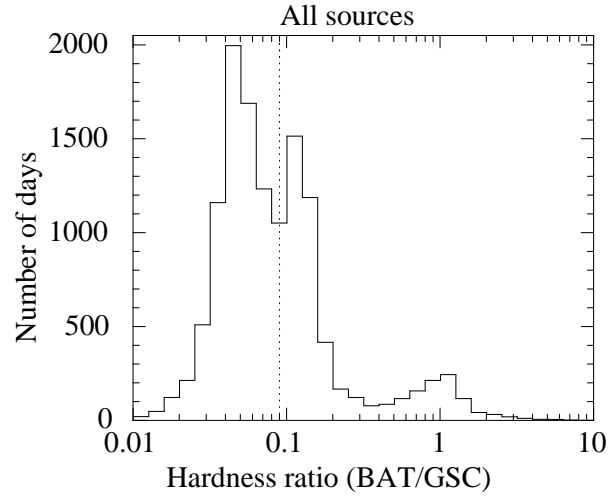
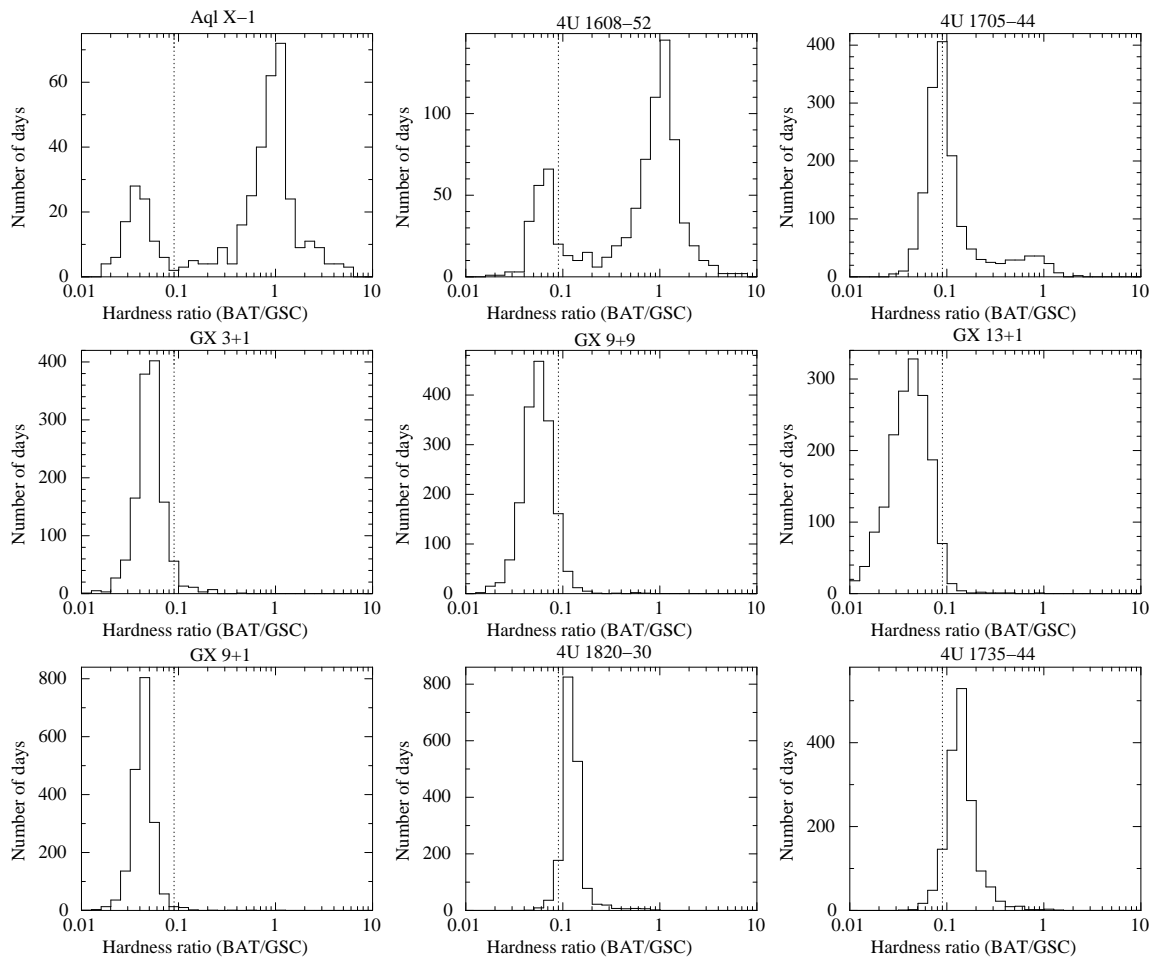


Fig. 3. Same as figure 1, but for GX 9+1, 4U 1820-30, and 4U 1735-44.



**Fig. 4.** Distributions of hardness ratios of BAT/GSC for all nine NS-LMXBs. The distributions were constructed from data with a significance  $> 1\sigma$ . The vertical dotted line represented the threshold between two soft states (see text for explanation).



**Fig. 5.** Distributions of hardness ratios of BAT/GSC for nine NS-LMXBs. The vertical dotted lines represented the threshold that we determined in figure 4.

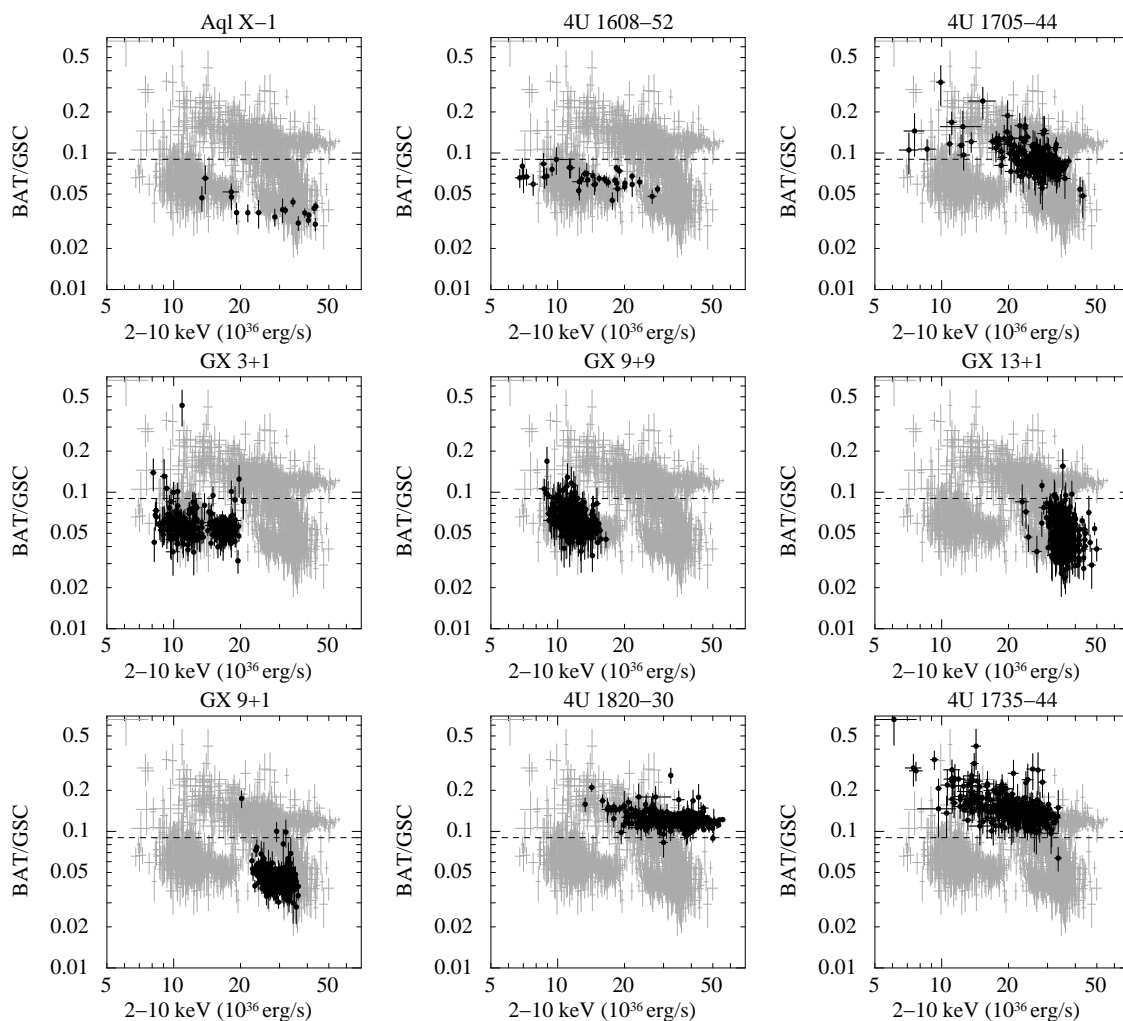


Fig. 6. Hardness–luminosity diagram, which plotted against a backdrop of all nine NS-LMXBs. The data are 5-d averaged. The distributions are constructed from data with a significance  $> 3\sigma$ . The horizontal dotted lines represented the the threshold that we determined in figure 4.

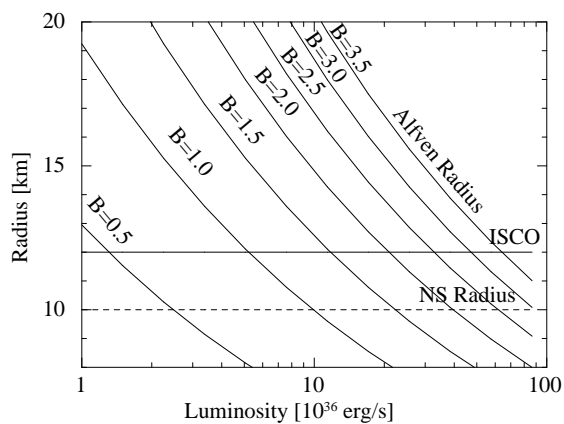
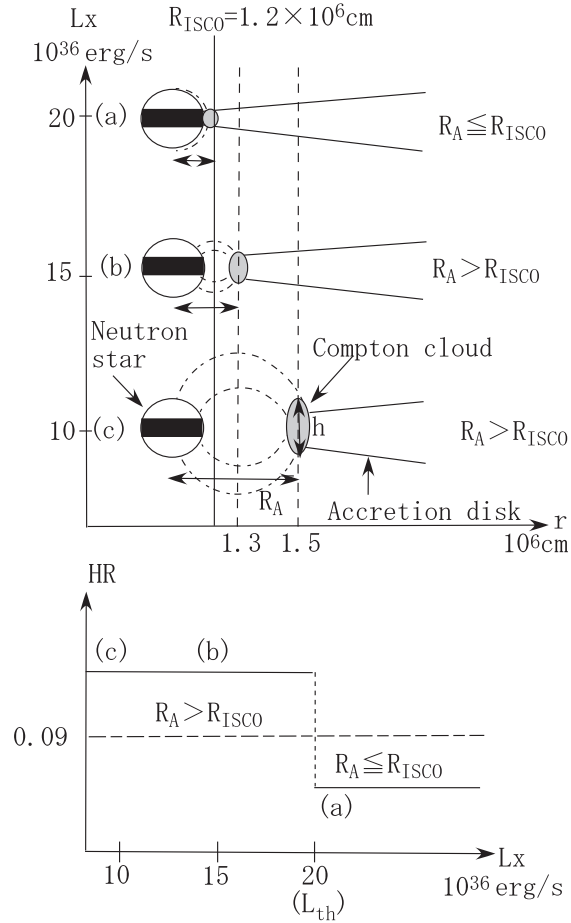
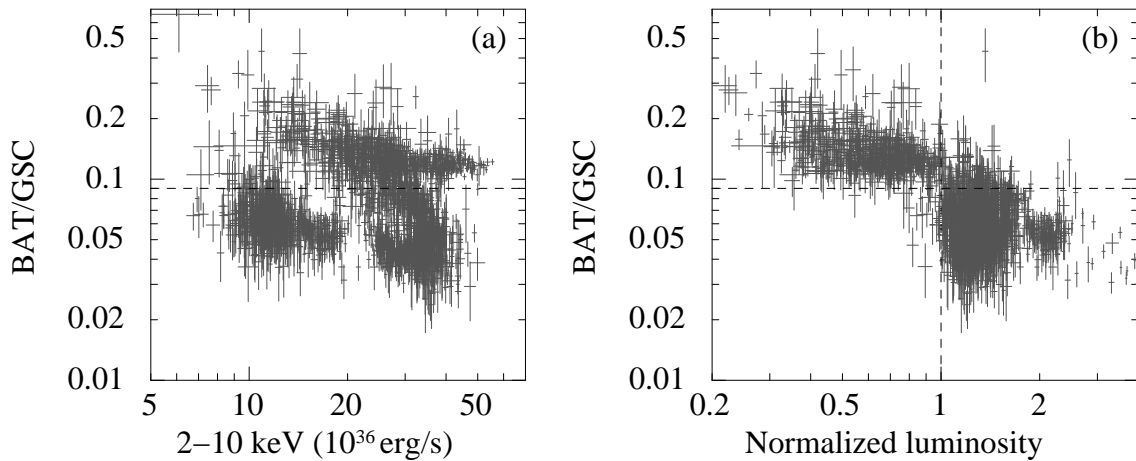


Fig. 7. Alfvén radius ( $R_A$ ) as a function of luminosity, where  $B$  is from  $0.5 \times 10^8$  G to  $3.5 \times 10^8$  G.



**Fig. 8.** Schematic drawings of suggesting geometry of NS-LMXB in the soft state. Assuming  $M_{\text{NS}} = 1.4M_{\odot}$  and  $B = 2 \times 10^8$  G, (a)  $R_A = 1.2 \times 10^6$  cm, (b)  $R_A = 1.3 \times 10^6$  cm, and (c)  $R_A = 1.5 \times 10^6$  cm corresponding to  $L = 20 \times 10^{36}$ ,  $15 \times 10^{36}$ , and  $10 \times 10^{36}$  erg  $\text{s}^{-1}$ , respectively. The HR representing the solid angle of the Compton cloud changed between (a) and (b), while it stays constant in (b) and (c).



**Fig. 9.** (a) Hardness–luminosity diagram for all the nine NS-LMXBs, which is the gray backdrop in figure 6. (b) Hardness–normalized luminosity diagram for all the nine NS-LMXBs (see text for explanation). The horizontal dotted lines in both panels represent the threshold that we determined in figure 4.

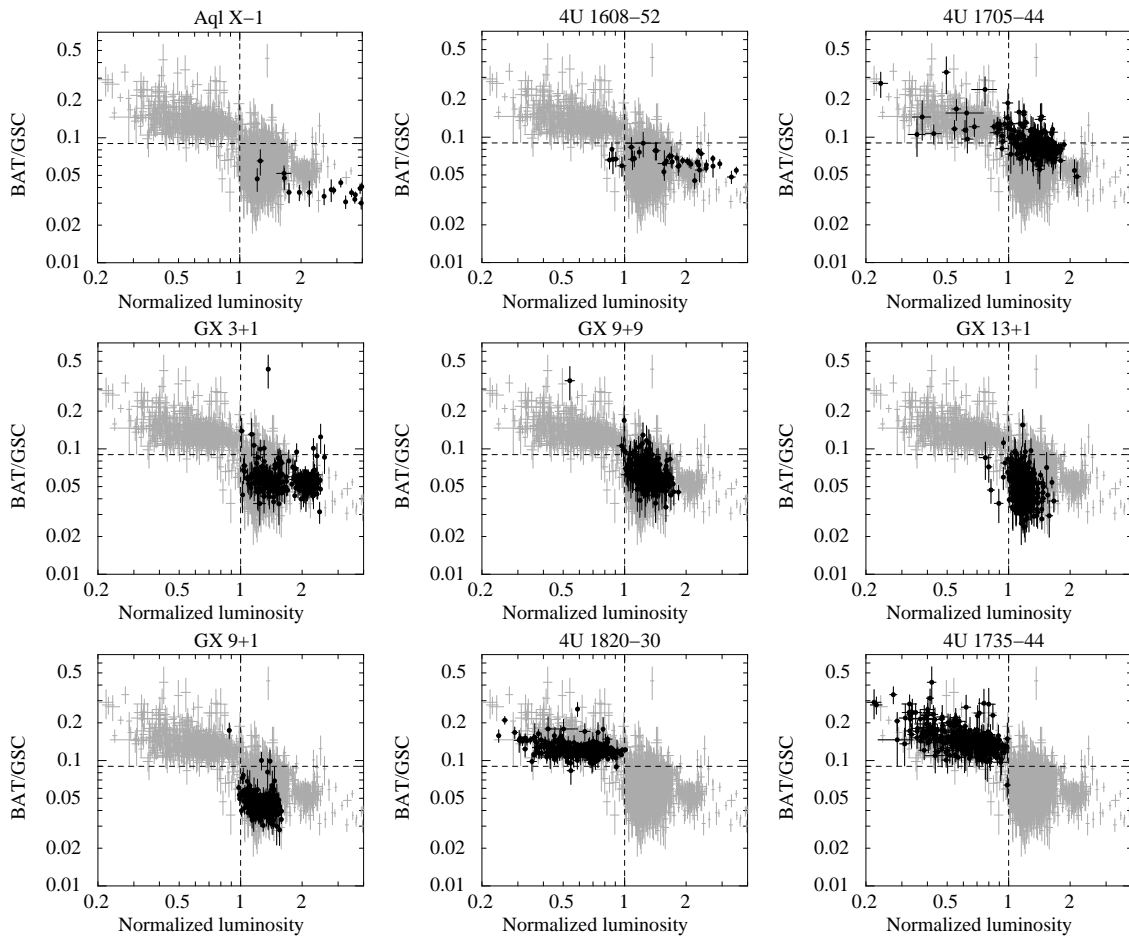


**Fig. 10.** Hardness–normalized luminosity diagram, which plotted against a backdrop of all the nine NS-LMXBs (figure 9b). The data are 5-d averaged. The distributions are constructed from data with a significance  $> 3\sigma$ . The horizontal dotted lines represent the threshold that we determined in figure 4.

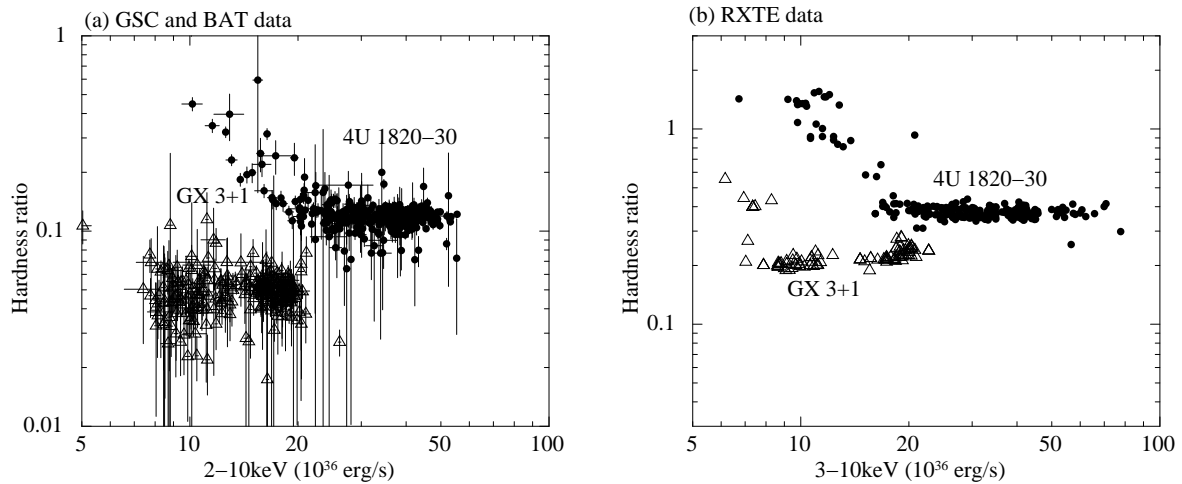


**Fig. 11.** Hardness–luminosity diagram of 4U 1820–30 and GX 3+1. The data of 4U 1820–30 included the data of both soft and hard state. (a) The data are obtained by GSC and BAT. The 2–10 keV luminosities are obtained by assuming Crab-like spectrum. The  $HR$  is 15–50 keV/2–10 keV. The data are 5-d average. (b) The data are obtained by RXTE, which is listed in table 4 of Titarchuk, Seifina, and Frontera (2013) for 4U 1820–30 and table 4 of Seifina and Titarchuk (2012) for GX 3+1. The  $HR$  of 4U 1820–30 and GX 3+1 is 10–50 keV/3–10 keV and 10–60 keV/3–10 keV, respectively.